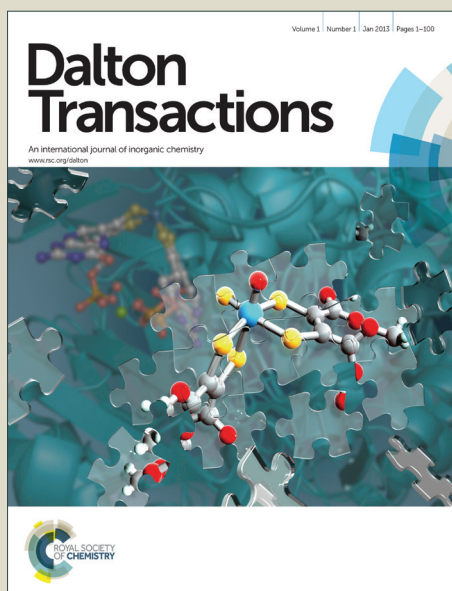


# Dalton Transactions

Accepted Manuscript



This is an *Accepted Manuscript*, which has been through the Royal Society of Chemistry peer review process and has been accepted for publication.

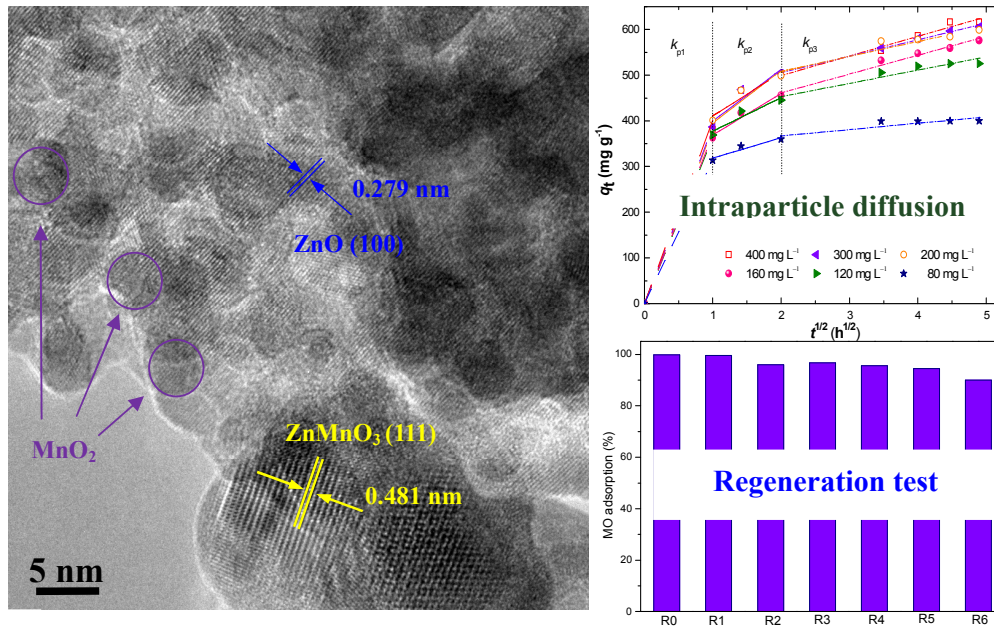
*Accepted Manuscripts* are published online shortly after acceptance, before technical editing, formatting and proof reading. Using this free service, authors can make their results available to the community, in citable form, before we publish the edited article. We will replace this *Accepted Manuscript* with the edited and formatted *Advance Article* as soon as it is available.

You can find more information about *Accepted Manuscripts* in the [Information for Authors](#).

Please note that technical editing may introduce minor changes to the text and/or graphics, which may alter content. The journal's standard [Terms & Conditions](#) and the [Ethical guidelines](#) still apply. In no event shall the Royal Society of Chemistry be held responsible for any errors or omissions in this *Accepted Manuscript* or any consequences arising from the use of any information it contains.



## Graphical Abstract



# MnO<sub>x</sub>-modified ZnAl-LDOs as high-performance adsorbent for the removal of methyl orange

Yu Xin Zhang<sup>a, b\*</sup>, Xiao Dong Hao<sup>a</sup>, Tian Wang<sup>a</sup>, Yu Xin Meng<sup>a</sup>, Xu Han<sup>c, d, e\*</sup>

## Abstract

MnO<sub>x</sub> modified ZnAl layered double oxides (M-LDO) nanocomposites were prepared through an intercalation/reduction/calcination process. The morphology and crystal structure of M-LDO were characterized by powder X-ray diffraction (XRD), transmission electron microscopy (TEM), Thermogravimetric analysis (TGA) and Fourier transform infrared spectroscopy (FT-IR) analysis methods. The results confirmed that the manganese oxides nanoparticles were well distributed on the LDO support. Methyl orange (MO) was chosen as a common water-soluble azo dye probe to evaluate the adsorption performance of M-LDO. The effects of MO initial concentration, agitation time, and temperature on MO adsorption were investigated. It was found that adsorption equilibrium data were best represented by the Langmuir and Redlich–Peterson isotherms and the maximum adsorption capacity was 617.28 mg g<sup>-1</sup> obtained from the Langmuir isotherm, which was much larger than some reported adsorbents. Besides, the adsorption process was spontaneous and endothermic in nature and followed pseudo-second-order kinetic model. The mechanism of the adsorption process was elaborated by intraparticle diffusion model. Moreover, the regeneration test of M-LDO was carried out and it showed that the used M-LDO was feasible for at least five times. In principle, this adsorbent with a high adsorption capacity and great reutilization performance could be very promising adsorbents for wastewater treatment.

**Keywords:** M-LDO nanocomposites, Methyl orange, Adsorption isotherms, Kinetics, Regeneration

## 1. Introduction

Wastewater produced from textile industries always contains high color, suspended solids and chemical oxygen demand (COD). It would cause enormous damage to the aquatic systems if discharged without further treatment. The removal of dyestuffs and pigments is of great concern since dyes and their degradation products are always carcinogens and toxic to human beings. Traditionally, various techniques including biological, physical and chemical methods have been applied in the removal process.<sup>1-3</sup> Adsorption has become the most popular

Manuscript submitted to *Dalton Transactions*

technique for dye removal due to its effectiveness, operational simplicity, low cost and low energy requirements.

In the past few years, many studies have used waste materials such as orange peel,<sup>4</sup> banana peel,<sup>4</sup> bottom ash,<sup>5</sup> de-oiled soya<sup>5</sup> as adsorbents for the removal of dyes. Nevertheless, adsorption capacity for these materials is always less than 20 mg g<sup>-1</sup>. Thus, it is therefore indispensable to develop novel adsorbents with high adsorption capacities.

Layered double hydroxides (LDHs), well-known anionic clays or hydrotalcite-like compounds have been widely used as low cost adsorbents.<sup>8, 9</sup> LDHs are represented by the general formula  $[M_{1-x}^{2+}M_x^{3+}(\text{OH})_2](A_{x/n}^{n-})_3 \cdot m\text{H}_2\text{O}$ , where  $M^{2+}$  and  $M^{3+}$  are the divalent and trivalent cations, respectively;  $A^{n-}$  is an interlayer anion;  $x$  is a ratio between divalent and trivalent cations.<sup>10</sup> Upon calcination, these LDHs compounds could produce intermediate non-stoichiometric mixed metal oxides with high specific surface area and homogeneous dispersion of metal cations. As adsorbents, layered double oxides (LDO) are receiving great interests due to their high anion retention capacities and simple thermal regeneration procedure, which was attributed to their unique “memory effect” properties.<sup>11, 12</sup> Until now, the adsorption behavior of hydrotalcite (both LDH and LDO) has been studied by many researchers.<sup>13-17</sup> For example, Ni *et al.*<sup>13</sup> reported that calcined layered double hydroxides (ZnAl-LDO) showed a maximum capacity of 181.9 mg g<sup>-1</sup> for the adsorption of methyl orange (MO) at equilibrium. It could be assumed that the adsorption performance would be improved by fine-tuning the preparation method and introduction of some more active ingredients. In our previous report, we had successfully fabricated the Au/ZnAl-LDO nanocomposites with a high maximum adsorption capacity of 625.17 mg g<sup>-1</sup> for the removal of MO in aqueous solution.<sup>18</sup> Although the introduction of gold element (only 1 wt.%) into ZnAl-LDH system significantly improved its adsorption performance, it was still expensive for broad application. Therefore, low cost ingredients instead of Au would be the promising candidate with the combination of ZnAl-LDO support for the purpose of exploring a cost-effective adsorbent in the field of wastewater treatment.

Manganese dioxides (MnO<sub>2</sub>) have attracted intensive interests because of their low cost, environmental compatibility and abundant availability.<sup>19-21</sup> Due to the existing unique layers or tunnels in lattices and high specific surface areas, manganese dioxides have been widely investigated and extensively used in adsorption processes.<sup>22-24</sup> In addition, the modification of other adsorbents with MnO<sub>2</sub> would actually improve their adsorption properties. For instance, the adsorbents prepared by the modification of diatomite with MnO<sub>2</sub>, with a higher adsorption capacity of about eight times as high as that of the raw diatomite for the removal of methylene blue has been reported.<sup>25-28</sup> Herein, we fabricated the MnO<sub>x</sub> modified ZnAl-LDO (M-LDO) nanocomposites and investigated their adsorption performance for the removal of MO. The adsorption efficiency of MO was studied

Manuscript submitted to *Dalton Transactions*

by optimizing experimental variables such as initial MO concentration, contact time, and temperature. The equilibrium and kinetic data of the adsorption process were then analyzed to study the adsorption isotherms, kinetics, thermodynamics and mechanism of MO on the prepared M-LDO. Moreover, the regeneration experiments of M-LDO were examined.

## 2. Materials and methods

### 2.1. Materials

Zinc nitrate ( $\text{Zn}(\text{NO}_3)_2 \cdot 6\text{H}_2\text{O}$ , 99%, Aladdin, Shanghai, China), aluminum nitrate ( $\text{Al}(\text{NO}_3)_3 \cdot 9\text{H}_2\text{O}$ , 99%, Aladdin, Shanghai, China), sodium borohydride ( $\text{NaBH}_4$ , 98%, Alfa Aesar), methyl orange ( $\text{C}_{14}\text{H}_{14}\text{N}_3\text{SO}_3\text{Na}$ , Alfa Aesar), ammonia ( $\text{NH}_3 \cdot \text{H}_2\text{O}$ , 25-28%, Chongqing Chuandong Chemical Co., Ltd, China), potassium permanganate ( $\text{KMnO}_4$ , 99.5%, Chongqing Chuandong Chemical Co., Ltd, China) were used in the synthesis without any further treatment.

### 2.2. Preparation of M-LDO nanocomposites

#### 2.2.1. Preparation of ZnAl-LDH precursors

ZnAl-LDH precursor with high Zn content was synthesized by a modified co-precipitation method.<sup>18,29</sup> Briefly, 20.0 mL of salt solution containing  $\text{Zn}(\text{NO}_3)_2 \cdot 6\text{H}_2\text{O}$  and  $\text{Al}(\text{NO}_3)_3 \cdot 9\text{H}_2\text{O}$  was added into a vigorously stirred ammonia solution (100.0 mL, 0.5 M) drop by drop. The total concentrations of cations were maintained at 1.0 M with the molar ratio of cations  $[\text{Al}^{3+}] / ([\text{Zn}^{2+}] + [\text{Al}^{3+}])$  of 0.13. After being aged at 338 K for 18 h, the mixture was then filtered and washed thoroughly with deionized water for three times, followed by redispersing the filter cake in deionized water for further use.

#### 2.2.2. Preparation of M-LDO nanocomposites

As-synthesized ZnAl-LDH precursor (100 mg) was dispersed in deionized water with the aid of ultrasonication, followed by dropwise adding of  $\text{KMnO}_4$  (0.01 M) aqueous solution with vigorous stirring and kept at 338 K for 24 h. The suspension was then washed thoroughly with deionized water. Thus,  $\text{MnO}_4^-$  anions were intercalated into the gallery of ZnAl-LDH during the anions exchange reaction. Afterwards, excessive freshly prepared  $\text{NaBH}_4$  aqueous solution was stirred with the  $\text{MnO}_4^-/\text{ZnAl-LDH}$  sample at room temperature for 4 h, and the solid product after washing with deionized water was marked as M-LDH. Finally, the dried M-LDH was calcined at 873 K for 2 h, which was marked as M-LDO.

### 2.3. Characterization

The crystallographic information and chemical composition of as-prepared samples were examined by powder X-ray diffraction (XRD, D/max 1200, Cu  $K_\alpha$ ) and Fourier transform infrared spectroscopy (FTIR, Nicolet 5DXC). The structural and morphological investigations of the samples were investigated by focused ion beam

Manuscript submitted to *Dalton Transactions*

scanning electron microscopy (FIB/SEM, ZEISS AURIGA) and transmission electron microscopy (TEM, ZEISS LIBRA 200). The thermal properties of M-LDH were determined using TGA (TGA/DSC 1/1100LF).

## 2.4. Batch equilibrium studies

Batch adsorption experiments were carried out in a set of Erlenmeyer flasks (250 mL) containing 100 mL of MO solutions with initial concentrations of 80–400 mg L<sup>-1</sup> together with 0.02 g of the as-prepared M-LDO. Then each flask was stirred at 303 K for 24 h to reach equilibrium. The samples were withdrawn at equilibrium to determine the residual concentrations subjected to the centrifugation at 5500 rpm for 5 min. The concentrations of MO in the supernatant before and after adsorption were determined using a double beam UV–visible spectrophotometer (UV-2450 Shimadzu, Japan) at 462 nm. Each experiment was conducted in duplicate under identical conditions. The amount of adsorption at equilibrium,  $q_e$  (mg g<sup>-1</sup>), was calculated by Eq. (1):

$$q_e = \frac{(C_0 - C_e)V}{M}$$

(1)

where  $C_0$  and  $C_e$  (mg L<sup>-1</sup>) are the liquid-phase concentrations of dye initially and at equilibrium, respectively.  $V$  is the volume of the solution (L) and  $M$  is the mass of dry adsorbent used (g).

### 2.4.1. Langmuir isotherm

Langmuir isotherm was based on the assumption of a homogeneous adsorbent surface with identical adsorption sites.<sup>30</sup> The linear form of Langmuir isotherm equation was given as by Eq. (2):<sup>31</sup>

$$\frac{C_e}{q_e} = \frac{1}{q_m K_L} + \frac{1}{q_m} C_e$$

(2)

where  $C_e$  was the equilibrium concentration of the adsorbate (mg L<sup>-1</sup>),  $q_e$  was the amount of adsorbate adsorbed per unit mass of adsorbent (mg g<sup>-1</sup>),  $q_m$  and  $K_L$  (L mg<sup>-1</sup>) are Langmuir constants related to adsorption capacity and rate of adsorption, respectively.

### 2.4.2. Freundlich isotherm

Freundlich isotherm on the other hand assumes heterogeneous surface energies, in which the energy term in Langmuir equation varied as a function of the surface coverage. The well-known logarithmic form of Freundlich isotherm was given by the following equation:<sup>32</sup>

$$\ln q_e = \ln K_F + \frac{1}{n} \ln C_e$$

(3)

where  $K_F$  and  $n$  were Freundlich constants with  $n$  giving an indication of how favorable the adsorption process and

Manuscript submitted to *Dalton Transactions*

$K_F$  ( $\text{mg}^{1-1/n} \text{L}^{1/n} \text{g}^{-1}$ ) was the adsorption capacity of the adsorbent.  $K_F$ , defined as the adsorption or distribution coefficient, represented the quantity of dye adsorbed onto M-LDO for a collection of equilibrium concentration.

#### 2.4.3. Redliche–Peterson isotherm

The Redliche–Peterson model was used as a compromise between the Langmuir model and Freundlich model (Fig. 6). It approached the Freundlich model at high concentration and its low concentration was in accordance with the limit of the Langmuir equation. In addition, the R–P equation combined three parameters into an empirical isotherm, and thus can be applied either in homogenous or heterogeneous systems because of the high versatility of the equation, which can be described as following equations:

$$q_e = \frac{K_R C_e}{1 + a_R C_e^\beta}$$

(4)

where,  $K_R$  ( $\text{L g}^{-1}$ ) and  $a_R$  ( $\text{L}^\beta \text{mg}^{-\beta}$ ), are R–P isotherm constants, and  $\beta$  is the exponent which lied between 1 and 0,

where  $\beta = 1$

$$q_e = \frac{K_R C_e}{1 + a_R C_e}$$

(5)

It becomes a Langmuir equation. Where  $\beta = 0$

$$q_e = \frac{K_R C_e}{1 + a_R}$$

(6)

i.e. the Henry's Law equation.

Eq. (4) can be converted to be a linear form as follows:

$$\ln\left(K_R \frac{C_e}{q_e} - 1\right) = \ln a_R + \beta \ln C_e$$

(7)

Because these three parameters ( $K_R$ ,  $a_R$ ,  $\beta$ ) cannot be solved from the linear equation on the basis of Eq. (7), the parameters cannot be determined using the linear forms by linearization. Hence, by minimising the distance between the experimental data points and the theoretical model predictions, the parameters of the equations could be obtained with the help of the solver add-in function of the Microsoft excel.<sup>33</sup>

## 2.5 Batch kinetics studies

The kinetic tests were carried out following the same procedure used for the equilibrium tests. Aqueous samples were taken at different intervals of time and the concentrations of MO were measured at the same intervals. The

Manuscript submitted to *Dalton Transactions*

MO uptake at a certain time,  $q_t$  (mg g<sup>-1</sup>), was calculated by Eq. (8):

$$q_t = \frac{(C_0 - C_t)V}{M}$$

(8)

where  $C_0$  and  $C_t$  (mg L<sup>-1</sup>) are the liquid-phase concentrations of dye initially and a certain time  $t$  (h), respectively.

$V$  is the volume of the solution (L) and  $M$  is the mass of dry adsorbent used (g).

### 2.5.1. Pseudo-first-order kinetic model

The non-linear pseudo-first order equation was given as:<sup>34</sup>

$$q_t = q_e(1 - e^{-k_1 t})$$

(9)

where  $q_e$  and  $q_t$  (mg g<sup>-1</sup>), are the amount of MO dye adsorbed at equilibrium and at a certain time  $t$  (h)

respectively;  $k_1$  (h<sup>-1</sup>), is the rate constant of adsorption.

### 2.5.2. Pseudo-second-order kinetic model

The pseudo-second order equilibrium adsorption model equation was given as:<sup>35</sup>

$$q_t = \frac{k_2 q_e^2 t}{(1 + k_2 q_e t)}$$

(10)

Eq. (10) can be converted to be a linear form as follows:

$$\frac{t}{q_t} = \frac{1}{k_2 q_e^2} + \frac{t}{q_e}$$

(11)

where  $k_2$  (g mg<sup>-1</sup> h) was the rate constant of second-order adsorption.

### 2.5.3. Intraparticle diffusion model

Weber and Morris<sup>36</sup> proposed the intraparticle diffusion model as a measurement to identify the diffusion mechanism. It was an empirically functional relationship, common to the most adsorption processes, where uptake varied almost proportionally with  $t^{1/2}$  rather than with the contact time  $t$ . According to this theory:

$$q_t = k_{pi} t^{1/2} + C_i$$

(12)

Where  $k_{pi}$  (mg g<sup>-1</sup> h<sup>1/2</sup>), the rate parameter of stage  $i$ , is obtained from the slope of the straight line of  $q_t$  versus  $t^{1/2}$

(Table 2; Fig. 8).  $C_i$ , the intercept of stage  $i$ .

## 2.6. Regeneration of M-LDO nanocomposites

Manuscript submitted to *Dalton Transactions*

In order to explore the potential reutilization of M-LDO nanocomposites as adsorbents for MO removal from aqueous solution, thermal regeneration tests were carried out by calcining the exhausted adsorbents.<sup>8</sup> Particularly, a portion of 0.13 g M-LDO nanocomposites was placed in 130 mg L<sup>-1</sup> of MO solution (100 mL) for the original use (R0). After completing equilibrium adsorption, the suspensions were recovered and calcined at 773 K for 1 h. The resulting material with a portion of 0.11 g was placed in 110 mg L<sup>-1</sup> MO solution (100 mL) for the first regeneration (R1). This procedure was repeated for another 5 times, resulting in six-cycle regeneration of M-LDO nanocomposites. The next five cycles were carried out by the addition of 0.09, 0.06, 0.04, 0.02, and 0.006 g of the regeneration materials to 90, 60, 40, 20, and 6 mg L<sup>-1</sup> of MO solution, which were marked as R2, R3, R4, R5, and R6, respectively.

### 3. Results and discussions

#### 3.1. Structure and morphology

Fig. 1 represents the crystalline phase of MnO<sub>4</sub><sup>-</sup>/ZnAl-LDH, M-LDH and M-LDO nanocomposites. Indeed, a series of (00*l*) harmonics at low angle were contributed to the characteristic diffraction peaks well-crystallized hydroxalcalite-like LDH materials (JCPDS no. 38-0486). Assuming a 3R stacking of the layers with the positions of the (003), (006) and (110) reflections, the lattice parameters including *a* and *c* could be calculated. The value of parameter *a* (= 2*d*<sub>110</sub>) was the average metal–metal distance in the interlayer structure (110), while *c* (=3*d*<sub>003</sub>=6*d*<sub>006</sub>) was a function of the average charge of the metal cations, the nature of the interlayer anion and the water content.<sup>37</sup>

Compared to the pristine ZnAl-LDH (See Supplementary Information, SI-1), the main characteristic (003) and (006) reflections of ZnAl-LDH shifted to high angle value after the intercalation of MnO<sub>4</sub><sup>-</sup> anions. The lattice parameter *c* was *ca.* 2.31 nm, decreasing from 2.72 nm of pristine ZnAl-LDH (SI-2). Meanwhile, the crystalline plane of ZnO phase was clearly depicted (JCPDS no. 36-1451) owing to the high amount of Zn content (Zn/Al=6.69:1).

When the MnO<sub>4</sub><sup>-</sup>/ZnAl-LDH samples were withdrawn after NaBH<sub>4</sub> reduction, the (003) and (006) reflections became broad and slightly shifted to low angle values, indicative of an increase in the lattice parameter *c*. The large loss of the intensity of all peaks suggested the less crystallinity of the reduced product, caused by the formation of MnO<sub>x</sub> modified ZnAl-LDH (M-LDH). An almost total decomposition of the original LDH layer structure after calcining M-LDH at 873 K for 2 h was verified since the (00*l*) peaks of M-LDO became disappeared (Fig. 1c). Interestingly, some weak diffraction peaks indexed with ZnMnO<sub>3</sub> compounds (JCPDS no. 19-1461) were observed on the spectrum of M-LDO. The formation of ZnMnO<sub>3</sub> was might be caused by sinter of ZnO and MnO<sub>2</sub> during the calcination process.<sup>38</sup>

Manuscript submitted to *Dalton Transactions*

TEM images of M-LDO nanocomposites (Fig. 2a-c) indicate that porous matrix of ZnAl-LDO with some gray phase was accomplished after the calcination process, different from the lamellar structure of the pristine ZnAl-LDH (SI-3). Energy dispersive X-ray (EDX) spectra confirm the existence of Mn element in the compound (SI-4). EDX line mapping also confirms that the distribution of Mn element was high in the gray phase along the pre-made line in the low magnification STEM image of M-LDO (Fig. 2c). The distribution trends of Zn and Mn element were nearly the same.

HRTEM images show that the lattice fringe of the lighter regions was 0.279 nm, which could be attributed to the (100) crystalline planes of ZnO phase. The larger lattice fringe of the darker regions (0.481 nm) can be indexed to the (111) crystalline planes of ZnMnO<sub>3</sub> compounds, in agreement with the XRD results. Besides, there were some nanoparticles with weak crystalline or amorphous phase lied under/upon the LDO layer support, which was attributed to manganese oxides, as were pointed in the circle region of Fig. 2c. Thereafter, we assumed that MnO<sub>4</sub><sup>-</sup> could be adsorbed on the excessive ZnO phase in the pristine LDH precursor as well as the ion exchange reaction, subjected to the process of reduction and calcinations, resulting in the formation of MnO<sub>2</sub> and/or ZnMnO<sub>3</sub>. The SAED pattern of M-LDO (Fig. 2d) shows that the distinctive diffraction spots could be indexed to the (100) and (110) planes of ZnO phase, while the other weak concentric diffraction rings were attributed to the ZnMnO<sub>3</sub> phases.

Typical FTIR spectra (Fig. 3) present that a strong band at 1384 cm<sup>-1</sup> corresponding to symmetric stretching band of NO<sub>3</sub><sup>-</sup> ions was observed in the spectra of the pristine ZnAl-LDH, indicative of NO<sub>3</sub><sup>-</sup>-type LDH. After intercalation/reduction/calcination processes, the adsorption band was weakened, and a new shoulder band at about 1356 cm<sup>-1</sup> appeared, which might be caused by the partial replacement of NO<sub>3</sub><sup>-</sup> with CO<sub>3</sub><sup>2-</sup> ions during the above procedure under atmospheric conditions, given that CO<sub>3</sub><sup>2-</sup> ion had a larger binding energy than NO<sub>3</sub><sup>-</sup> ion between the metal hydroxide layers and interlayer anions.<sup>39</sup> In addition, the lattice vibration bands from the M–O and O–M–O (M=Zn, Al) groups appeared in the 400–800 cm<sup>-1</sup> region. Specially, the weak adsorption band at 620 cm<sup>-1</sup> appeared at the spectra of the M-LDH and M-LDO, indicative of the formation of manganese oxide.<sup>40</sup> Moreover, the adsorption bands centered at 3460 and 1634 cm<sup>-1</sup> were corresponded to the surface-adsorbed water.

TGA/DSC test was conducted and the result was depicted in Fig. 4. It was evinced that two steps of weight loss occurred during the calcination process. The first decomposition step ended at 520 K, with a weight loss of 7.73% corresponding to the removal of interlayer water and water molecules. An 11.6% weight change in the second stage (520–900 K) was corresponded to the dehydroxylation of the layers and the loss of the interlayer ions.<sup>41</sup> The total weight loss percentage of M-LDH during 300-900 K was 19.33%. In the DSC profile, there

Manuscript submitted to *Dalton Transactions*

were two distinct endothermic peaks, centered at 606.20 K and 825.84 K, respectively. The first one was attributed to the dehydroxylation of the ZnAl-LDH layers, while the second one was attributed to formation of thermal transformation of manganese oxide.

### 3.2. Effect of contact time and initial dye concentration on adsorption equilibrium

Prior to the adsorption tests, the M-LDO samples at various conditions were used to evaluate the effect of calcination process on the adsorption properties of MO (SI-5). Accordingly, the optimized calcination condition of 873 K for 2 h was utilized to obtain M-LDO adsorbent in the adsorption equilibrium. Besides, the adsorption behavior of LDO and M-LDO were presented in SI-6. It proved that the presence of  $\text{MnO}_x$  oxides strongly improved the adsorption performance of ZnAl-LDO.

Fig.5 shows the adsorption capacity versus the adsorption time at various initial MO concentrations at 303 K. The results revealed that the MO adsorption was fast at the initial contact time, and thereafter it became slower near the equilibrium. It indicated that the contact time for MO solutions with initial concentrations of 80 and 120  $\text{mg L}^{-1}$  to reach equilibrium ranged between 4 and 12 h, while equilibrium time of 24 h was required for the higher initial concentrations of 160–400  $\text{mg L}^{-1}$  MO solutions. A mass of vacant surface sites were available for adsorption at the initial stage, and the remaining vacant surface sites were difficult to be occupied after a period of time due to repulsive forces between the solute molecules on the solid and bulk phases. It was evident that the amount of MO adsorbed onto the M-LDO increased as time went by, and at some point it reached a constant value beyond which no more MO was further removed from the solution. The amount of dye adsorbed at the equilibrium time reflected the maximum adsorption capacity of the adsorbent under those operating conditions. The adsorption capacity at equilibrium ( $q_e$ ) increased from 399.96 to 616.64  $\text{mg g}^{-1}$  with an increase in the initial dye concentrations from 80 to 400  $\text{mg L}^{-1}$ .

### 3.3. Adsorption isotherms

The adsorption isotherm revealed how the adsorption molecules distribute between the liquid phase and the solid phase at equilibrium state during the adsorption process. The analysis of the isotherm data by fitting them to different isotherm models was an important step to find the suitable model that can be used for design purposes.<sup>42</sup> Adsorption isotherm was important not only to describe how solutes interact with adsorbents, but also to optimize the use of adsorbents. Many kinds of isotherm equations have been widely used to describe the equilibrium nature of adsorption such as Langmuir, Freundlich and Redlich-Peterson isotherm models.<sup>43</sup>

For the Langmuir isotherm, the plot of  $C_e/q_e$  versus  $C_e$  in Fig. 6a shows a straight line with a coefficient of 0.9996 which indicates that the adsorption of MO onto the M-LDO fits the Langmuir isotherm reasonably well. The Langmuir constants  $K_L$  and  $q_m$  were calculated (Table 1). The essential characteristics of Langmuir isotherm

Manuscript submitted to *Dalton Transactions*

can be expressed by a dimensionless constant called separation factor or equilibrium parameter,  $R_L$ , which was defined as:<sup>30</sup>

$$R_L = \frac{1}{1 + C_0 K_L}$$

where  $K_L$  was the Langmuir constant and  $C_0$  was the highest dye concentration ( $\text{mg L}^{-1}$ ). The value of  $R_L$  determined the type of the isotherm to be either favorable ( $0 < R_L < 1$ ), unfavorable ( $R_L > 1$ ), linear ( $R_L = 1$ ) or irreversible ( $R_L = 0$ ). The value of  $R_L$  was found to be 0.0059 at 303 K, which further confirmed that the Langmuir isotherm model was favorable for adsorption of MO onto the M-LDO.

In the case of Freundlich isotherm, the  $\ln q_e$  versus  $\ln C_e$  plot in Fig. 6b displays a straight line with a correlation coefficient of 0.9709. The slope of  $1/n$  ranging between 0 and 1 was a measure of adsorption intensity or surface heterogeneity, becoming more heterogeneous as its value got closer to zero. A value for  $1/n$  below one revealed a normal Langmuir isotherm while  $1/n$  above one was indicative of cooperative adsorption<sup>44</sup>. The plot of  $\ln q_e$  versus  $\ln C_e$  showed a straight line with slope of  $1/n$  with value of 0.0707 (Fig. 6b), indicating a normal Langmuir isotherm. Accordingly, Freundlich constants  $K_F$  and  $n$  were calculated by Eq.(5) and their values were listed in Table 1.

The linearised form of the R-P isotherm plots for the adsorption data of MO onto the M-LDO at 303 K were presented in Fig. 6c and the values of  $K_R$ ,  $a_R$ ,  $\beta$  and the correlation coefficient,  $R^2$ , were listed in Table 1. Combining the advantages of Langmuir and Freundlich equations, R-P equation can be applied either in homogeneous or heterogeneous system. In this study, the  $\beta$  values were very close to 1, which implied that the isotherms conformed to Langmuir model better than Freundlich model, as in agreement with the conclusion listed above. Fig. 6d showed the comparison of experimental and predicted amount of MO adsorbed onto M-LDO for all the isotherm models investigated.

### 3.4. Adsorption kinetics

The kinetic of adsorption was utilized to describe the rate of MO onto the M-LDO and control the equilibrium time. The pseudo-first-order kinetic model and pseudo-second-order kinetic models were applied to study the kinetics of the adsorption process while the intraparticle diffusion model was utilized to determine the diffusion mechanism of the adsorption system. The kinetics parameters and correlation coefficient values of the pseudo-first-order kinetic and pseudo-second-order kinetic models are listed in SI-7. The linear plot of  $t/q_t$  versus  $t$  in Fig. 7 shows a good agreement between the experimental and the calculated  $q_e$  values. Besides, the correlation coefficient values for the second-order kinetic model were almost equal to 1 for all MO concentrations, indicating the applicability of the second-order kinetic model to describe the adsorption process

Manuscript submitted to *Dalton Transactions*

of MO on the prepared M-LDO.

Moreover, the intraparticle diffusion model<sup>36</sup> is often selected as a measurement to identify the diffusion mechanism. It was an empirically functional relationship, common to the most adsorption processes, where uptake varied almost proportionally with  $t^{1/2}$  rather than with the contact time  $t$ . The sorption rate was known to be controlled by several factors including: (i) film diffusion, where adsorbate ions travelled towards the external surface of the adsorbent; (ii) particle diffusion, where adsorbate ions travelled within the pores of the adsorbent excluding a small amount of adsorption that occurred on the exterior surface of the adsorbent; (iii) adsorption of the adsorbate ions on the interior surface of the adsorbent.<sup>45,46</sup> For intraparticle diffusion plots, the first sharper region was the instantaneous adsorption or external surface adsorption; the second region became a gradual adsorption stage due to intraparticle diffusion; the third region was the final equilibrium stage where intraparticle diffusion started to slow down since that there remained extremely low adsorbate concentrations in the solutions.<sup>47</sup> Fig. 8 showed that the first stage was completed within the first 1 h for all initial concentrations. This was attributed to external surface adsorption, in which the adsorbate diffused through the bulk solution to the external surface of the adsorbent or the boundary layer diffusion of MO molecules. There followed the second adsorption stage, where intraparticle diffusion rate was rate controlling. The plots did not pass through the origin,  $C_2 \neq 0$ , indicating that the intraparticle diffusion was involved in the adsorption process, but was not the only rate-controlling step. Also,  $C$  value gave an idea about the thickness of boundary layer, i.e., the larger the intercept, the greater the boundary layer effect.<sup>48</sup> A deeper understanding was also given by the boundary layer about the tendency of the solid to adsorb onto the adsorbent phase or remain in solution. Since diffusion took place, the boundary layer was treated as a viscous drag existing between the M-LDO surface and the MO solution diffusing across its surface. Therefore, higher values of  $C$ , i.e. the boundary layer thickness, depicted higher adsorption capacities.

### 3.5. Adsorption thermodynamic

In an isolated system where energy cannot be gained or lost, the concept of thermodynamic assumed that the entropy change was the driving force.<sup>49</sup> The thermodynamic parameters that must be considered to determine the adsorption processes were changes in standard enthalpy ( $\Delta H^\circ$ ), standard free energy ( $\Delta G^\circ$ ), standard entropy ( $\Delta S^\circ$ ) due to transfer of unit mole of solute from solution onto the solid–liquid interface. The value of  $\Delta H^\circ$  and  $\Delta S^\circ$  can be computed using the following equation:

$$\Delta G^\circ = -RT \ln K_d$$

(10)

Manuscript submitted to *Dalton Transactions*

$$\ln K_d = \frac{\Delta S^\circ}{R} - \frac{\Delta H^\circ}{RT}$$

(11)

$$K_d = \frac{C_{Ae}}{C_e}$$

(12)

where  $R$  (8.314 J mol<sup>-1</sup> K) is the universal gas constant,  $T$  (K) is the absolute temperature and  $K_d$  is the distribution coefficient;  $C_{Ae}$  (mg g<sup>-1</sup>) is the amount adsorbed on solid at equilibrium and  $C_e$  (mg L<sup>-1</sup>) was the equilibrium concentration. The values of these thermodynamic parameters (studied at three different temperatures) were listed in Table 3. With increasing temperature, the decrease in  $\Delta G^\circ$  values indicated an increase in the feasibility and spontaneity of the adsorption at higher temperatures.

The positive  $\Delta H^\circ$  value indicated the endothermic nature of the adsorption. The positive value of  $\Delta S^\circ$  indicated that there was increased randomness at the solid–solution interface during the adsorption of MO in aqueous solution on M-LDO. Some structural changes may have taken place as a result of interactions between the MO molecules and the functional groups on the M-LDO surface.<sup>50</sup>

### 3.6. Regeneration of M-LDO nanocomposites

Thermal regeneration tests were carried out by calcining the exhausted adsorbents, aiming at exploring the potential reutilization of M-LDO nanocomposites as adsorbents for MO removal from aqueous solution.<sup>8</sup> Adsorption of MO used for the regenerated M-LDO after six times of thermal recycling was shown in Fig. 9. The reduction of the percentage of MO adsorption was small for the first five regenerations (R1–R5), ranging between 0.2–5.3%, compared with the original M-LDO (R0). It was probably due to the fact that LDO were capable of being regenerated based on the “memory effect”, that is, LDO compounds can easily reconstruct the original layered structure in an anionic solution.<sup>13</sup> The XRD spectrum of the M-LDO after the adsorption of MO proves that M-LDO could also be restored during the adsorption process (SI-8). Nevertheless, the percentage of MO adsorption for the sixth cycle depicted a larger decrease compared to the first five regenerations. These results revealed that the thermal regeneration of the used LDO for reuse was feasible only within the first five cycles, after which the regenerated materials will suffer from a large loss in their adsorption capacities. During the regeneration process in addition to poor crystallinity of LDHs materials, as discussed in the previous reports, the large loss for the Au/ZnAl-LDO nanocomposites of adsorption capability may be attributed to damage of the original layered structure).<sup>13,51</sup> Besides, the XRD spectrum of M-LDO after the adsorption of MO for the five regenerations indicated that the “memory effect” of M-LDO was weakened and disappeared, leading to a larger loss of the adsorption capacity (SI-9). However, the percentage of MO removal for M-LDO (R6) was 90.01%,

Manuscript submitted to *Dalton Transactions*

which was still a high adsorption performance. These results suggested that the thermal regeneration of the used M-LDO for reutilized was feasible for at least five cycles.

#### 4. Conclusions

In summary, we have successfully synthesized  $\text{MnO}_x$  modified ZnAl-LDH through an intercalation/reduction process. Afterwards, calcination procedures were optimized to obtain  $\text{MnO}_x$  modified ZnAl-LDO (M-LDO) as adsorbent for the removal of MO. Equilibrium data were fitted by Langmuir, Freundlich and Redlich-Peterson isotherms and the data were better described by Langmuir isotherm, with a maximum adsorption capacity of  $617.28 \text{ mg g}^{-1}$  for M-LDO nanocomposites, which was much larger than some other adsorbents. Moreover, thermal regeneration for reuse of M-LDO as adsorbent after MO adsorption could be feasible at least for five 5 times (94.4% retained). In principle, these findings suggested that M-LDO nanocomposites could be widely and potentially used in dye wastewater treatment.

#### Acknowledgments

The authors gratefully acknowledge the financial supports provided by National Natural Science Foundation of China (Grant no. 51104194 and 41373114), Doctoral Fund of Ministry of Education of China (20110191120014), No. 43 Scientific Research Foundation for the Returned Overseas Chinese Scholars, National Key laboratory of Fundamental Science of Micro/Nano-device and System Technology (2013MS06, Chongqing University), State Education Ministry and Fundamental Research Funds for the Central Universities (Project no. CDJZR12248801, CDJZR12135501, and CDJZR13130035, Chongqing University, PR China). Support from Open Funding Project of the Key Laboratory of Systems Bioengineering, Ministry of Education is also acknowledged.

#### Notes and references

<sup>a</sup>College of Materials Science and Engineering, Chongqing University, Chongqing 400044, P.R. China

<sup>b</sup>National Key Laboratory of Fundamental Science of Micro/Nano-Devices and System Technology, Chongqing University, Chongqing 400044, P.R. China

<sup>c</sup>State Key Laboratory of Hollow Fiber Membrane Materials and Processes, Tianjin Polytechnic University, Tianjin 300387, P.R. China

<sup>d</sup>School of Environmental and Chemical Engineering, Tianjin Polytechnic University, Tianjin 300387, P.R. China

<sup>e</sup>Key Laboratory of Systems Bioengineering, Ministry of Education, Tianjin University, Tianjin 300072, P.R. China

\* Corresponding author. Tel.: +86 23 65104131; Fax: +86 23 65104131

E-mail: zhangyuxin@cqu.edu.cn (Y.X. Zhang); hanxu\_mail2013@163.com (X. Han)

† Electronic supplementary information (ESI) available.

1. K. Swaminathan, S. Sandhya, A. Carmalin Sophia, K. Pachhade and Y. V. Subrahmanyam, *Chemosphere*, 2003, **50**, 619-625.

Manuscript submitted to *Dalton Transactions*

2. C. O'Neill, F. R. Hawkes, D. L. Hawkes, S. Esteves and S. J. Wilcox, *Water Research*, 2000, **34**, 2355-2361.
3. C. A. K. Gouvea, F. Wypych, S. G. Moraes, N. Duran, N. Nagata and P. Peralta-Zamora, *Chemosphere*, 2000, **40**, 433-440.
4. G. Annadurai, R. S. Juang and D. J. Lee, *J. Hazard. Mater.*, 2002, **92**, 263-274.
5. A. Mittal, A. Malviya, D. Kaur, J. Mittal and L. Kurup, *J. Hazard. Mater.*, 2007, **148**, 229-240.
6. K. Nakagawa, A. Namba, S. R. Mukai, H. Tamon, P. Ariyadejwanich and W. Tanthapanichakoon, *Water Research*, 2004, **38**, 1791-1798.
7. P. C. C. Faria, J. J. M. Órfão and M. F. R. Pereira, *Water Research*, 2004, **38**, 2043-2052.
8. E. L. Crepaldi, J. Tronto, L. P. Cardoso and J. B. Valim, *Colloid Surf. A-Physicochem. Eng. Asp.*, 2002, **211**, 103-114.
9. L. Lv, J. He, M. Wei and X. Duan, *Industrial and Engineering Chemistry Research*, 2006, **45**, 8623-8628.
10. F. Cavani, F. Trifirò and A. Vaccari, *Catalysis Today*, 1991, **11**, 173-301.
11. S. Tezuka, R. Chitrakar, K. Sakane, A. Sonoda, K. Ooi and T. Tomida, *Bull. Chem. Soc. Jpn.*, 2004, **77**, 2101-2107.
12. Q. H. Hu, Z. P. Xu, S. Z. Qiao, F. Haghseresht, M. Wilson and G. Q. Lu, *J. Colloid Interface Sci.*, 2007, **308**, 191-199.
13. Z. M. Ni, S. J. Xia, L. G. Wang, F. F. Xing and G. X. Pan, *J. Colloid Interface Sci.*, 2007, **316**, 284-291.
14. X. H. Liu, J. Zhang, X. Z. Guo, S. H. Wu and S. R. Wang, *Nanotechnol.*, 2010, **21**, 095501-095508.
15. D. D. Asouhidou, K. S. Triantafyllidis, N. K. Lazaridis and K. A. Matis, *Journal of Chemical Technology & Biotechnology*, 2012, **87**, 575-582.
16. L. Ai, C. Zhang and L. Meng, *Journal of Chemical & Engineering Data*, 2011, **56**, 4217-4225.
17. D. Chen, Y. Li, J. Zhang, J.-z. Zhou, Y. Guo and H. Liu, *Chem. Eng. J.*, 2012, **185-186**, 120-126.
18. Y. X. Zhang, X. D. Hao, M. Kuang, H. Zhao and Z. Q. Wen, *Appl. Surf. Sci.*, 2013, **283**, 505-512.
19. Z. Liu, Y. Xing, C.-H. Chen, L. Zhao and S. L. Suib, *Chem. Mater.*, 2008, **20**, 2069-2071.
20. S. Shanmugam and A. Gedanken, *The Journal of Physical Chemistry B*, 2006, **110**, 24486-24491.
21. K. Gong, P. Yu, L. Su, S. Xiong and L. Mao, *J. Phys. Chem. C*, 2007, **111**, 1882-1887.
22. J. Yu, R. Chen and W. Xiao, *J. Mater. Chem. A*, 2013, **1**, 11682-11690.
23. J. B. Fei, Y. Cui, X. H. Yan, W. Qi, Y. Yang, K. W. Wang, Q. He and J. B. Li, *Adv. Mater.*, 2008, **20**, 452-456.
24. J. Ge and J. Qu, *J. Hazard. Mater.*, 2003, **100**, 197-207.
25. M. A. Al-Ghouti, Y. S. Al-Degs, M. A. Khraisheh, M. N. Ahmad and S. J. Allen, *J. Environ. Manage.*, 2009, **90**, 3520-3527.
26. M. A. Al-Ghouti, M. A. Khraisheh, M. N. Ahmad and S. J. Allen, *J. Hazard. Mater.*, 2007, **146**, 316-327.
27. J. X. Lin, S. L. Zhan, M. H. Fang and X. Q. Qian, *Journal of Porous Materials*, 2007, **14**, 449-455.
28. R. Shawabkeh, *Applied Clay Science*, 2003, **24**, 111-120.
29. Z. P. Xu and H. C. Zeng, *The Journal of Physical Chemistry B*, 2001, **105**, 1743-1749.
30. T. W. Weber and R. K. Chakravorti, *Aiche J.*, 1974, **20**, 228-238.
31. I. Langmuir, *J. Am. Chem. Soc.*, 1918, **40**, 1361-1403.
32. H. Freundlich, *J. Phys. Chem.*, 1906, **57**, 385-470.
33. Y. C. Wong, Y. S. Szeto, W. H. Cheung and G. McKay, *Process Biochemistry*, 2004, **39**, 695-704.
34. M. Toor and B. Jin, *Chem. Eng. J.*, 2012, **187**, 79-88.
35. Y. S. Ho and G. McKay, *Process Biochemistry*, 1999, **34**, 451-465.
36. I. A. Tan, A. L. Ahmad and B. H. Hameed, *J. Hazard. Mater.*, 2009, **164**, 473-482.
37. D. G. Evans and R. C. T. Slade, *Stuct Bond*, 2006, **119**, 1-87.
38. C. Cong, L. Liao, Q. Liu, J. Li and K. Zhang, *Nanotechnol.*, 2006, **17**, 1520-1526.
39. S. Ma, C. Fan, L. Du, G. Huang, X. Yang, W. Tang, Y. Makita and K. Ooi, *Chem. Mater.*, 2009, **21**, 3602-3610.
40. P. Zhang, X. Li, Q. Zhao and S. Liu, *Nanoscale Res. Lett.*, 2011, **6**, 1-8.
41. Y. Yan, Q. Liu, J. Wang, J. Wei, Z. Gao, T. Mann, Z. Li, Y. He, M. Zhang and L. Liu, *J. Colloid Interface Sci.*, 2012, **371**, 15-19.
42. M. El-Geundi, *Adsorption science and technology*, 1991, **8**, 217-225.
43. O. Redlich and D. L. Peterson, *Journal of Physical Chemistry*, 1959, **63**, 1024-1024.
44. K. Fytianos, E. Voudrias and E. Kokkalis, *Chemosphere*, 2000, **40**, 3-6.
45. O. Gerçel, A. Özcan, A. S. Özcan and H. F. Gerçel, *Appl. Surf. Sci.*, 2007, **253**, 4843-4852.
46. F. C. Wu, R. L. Tseng and R. S. Juang, *Water Research*, 2001, **35**, 613-618.
47. F. C. Wu, R. L. Tseng and R. S. Juang, *J. Colloid Interface Sci.*, 2005, **283**, 49-56.
48. A. S. Özcan, B. Erdem and A. Özcan, *Colloids and Surfaces A: Physicochemical and Engineering Aspects*, 2005, **266**, 73-81.
49. K. V. Kumar and A. Kumaran, *Biochem. Eng. J.*, 2005, **27**, 83-93.
50. S. Senthilkumar, P. Kalaamani, K. Porkodi, P. R. Varadarajan and C. V. Subburaam, *Bioresource*

Manuscript submitted to *Dalton Transactions*

---

- Technol.*, 2006, **97**, 1618-1625.
51. M. Ulibarri, I. Pavlovic, C. Barriga, M. Hermosin and J. Cornejo, *Applied Clay Science*, 2001, **18**, 17-27.

**Table and Figures Captions**

**Table 1.** Langmuir, Redlich–Peterson, Freundlich isotherm model constants and coefficients for adsorption of MO on M-LDO at 303 K.

**Table 2.** Intraparticles diffusion model constants and coefficients of MO adsorption on M-LDO at 303 K.

**Table 3.** Thermodynamic parameters for adsorption of MO on M-LDO at 303 K.

**Fig.1.** XRD patterns of (a)  $\text{MnO}_4^-/\text{ZnAl-LDH}$  ( $\text{MnO}_4^-$  anions intercalated ZnAl-LDH), (b) M-LDH (after the  $\text{NaBH}_4$  reduction of  $\text{MnO}_4^-/\text{ZnAl-LDH}$ ), and (c) M-LDO (obtained by calcining M-LDH at 873 K for 2 h).

**Fig.2.** (a, b) Low and (c) high magnification TEM images of M-LDO nanocomposites; (d) the corresponding SAED patterns of M-LDO nanocomposites.

**Fig.3.** FT-IR spectra of (a) pristine ZnAl-LDH, (b)  $\text{MnO}_4^-$  intercalated ZnAl-LDH, (c)  $\text{MnO}_2/\text{ZnAl-LDH}$  (M-LDH) and (d)  $\text{ZnMnO}_3/\text{ZnAl-LDO}$  (M-LDO) nanocomposites.

**Fig.4.** TGA-DSC curves of M-LDH nanocomposites.

**Fig.5.** Effect of contact time on MO adsorption on M-LDO nanocomposites at various initial concentrations ( $80\text{--}400\text{ mg L}^{-1}$ ) at 303 K.

**Fig.6.** Adsorption isotherms of MO onto M-LDO at 303 K for different models: a) Langmuir model, b) Freundlich model and c) Redlich-Peterson model. (d) the comparison of experimental and predicted amount of MO adsorbed onto M-LDO for the isotherms models studied.

**Fig.7.** Pseudo-second-order kinetics for adsorption of MO onto M-LDO at 303 K.

**Fig.8.** Plot of intraparticle diffusion model for adsorption of MO onto M-LDO at 303 K.

**Fig.9.** Comparison of MO adsorption between M-LDO (R0) and thermally regenerated materials from used M-LDO. R1, R2, R3, R4, R5 and R6 are the corresponding reused products after a six-cycle thermal regeneration process.

Manuscript submitted to *Dalton Transactions***Table 1**

Langmuir constants	$K_L$ (L mg <sup>-1</sup> ) 0.4263	$q_m$ (mg g <sup>-1</sup> ) 617.2840	$R_L$ 0.0058	$R^2$ 0.9996
Redlich-Peterson constants	$K_R$ (L mg <sup>-1</sup> ) 189.3225	$a_R$ ((L <sup><math>\beta</math></sup> mg <sup>-<math>\beta</math></sup> ) 3.3990	$\beta$ 0.9889	$R^2$ 0.9999
Freundlich constants	$K_F$ (mg <sup>1-1/n</sup> L <sup>1/n</sup> g <sup>-1</sup> ) 426.6227		1/n 0.0707	$R^2$ 0.9709

Manuscript submitted to *Dalton Transactions*

Table 2

$C_0$ (mg L <sup>-1</sup> )	Intraparticle diffusion model								
	$k_{p1}$ (mg g <sup>-1</sup> h <sup>1/2</sup> )	$k_{p2}$ (mg g <sup>-1</sup> h <sup>1/2</sup> )	$k_{p3}$ (mg g <sup>-1</sup> h <sup>1/2</sup> )	$C_1$	$C_2$	$C_3$	$(R_1)^2$	$(R_2)^2$	$(R_3)^2$
80	313.8146	45.0262	13.8731	0	273.2813	399.2223	1	0.8398	0.7216
120	369.29802	73.3018	29.0602	0	304.0885	394.6962	1	0.8073	0.8923
160	362.9593	90.7952	41.1361	0	278.4052	379.0603	1	0.9207	0.97088
200	400.9452	94.965	32.5889	0	315.7275	443.2182	1	0.8313	0.9095
300	386.8714	113.0409	36.0699	0	286.5709	433.1836	1	0.8001	0.9935
400	381.2651	115.8256	42.7683	0	279.1088	413.7161	1	0.7829	0.96624

Manuscript submitted to *Dalton Transactions***Table 3**

$C_0$ (mg L <sup>-1</sup> )	$\Delta H^\circ$ (kJ mol <sup>-1</sup> )	$\Delta S^\circ$ (kJ mol <sup>-1</sup> )	$\Delta G^\circ$ (kJ mol <sup>-1</sup> )		
			303 K	313 K	328 K
400	1.9347	0.0600	-16.2493	-16.8523	-17.7499

Fig. 1

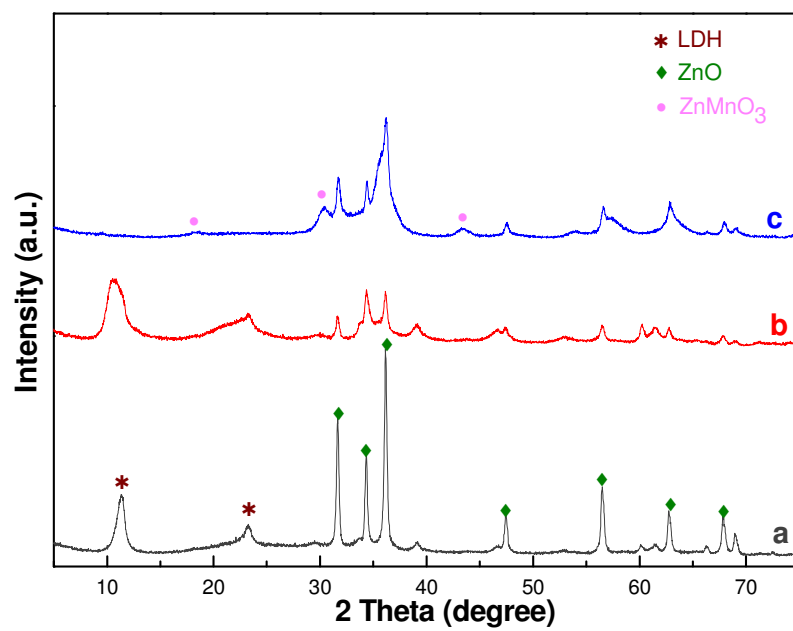


Fig. 2

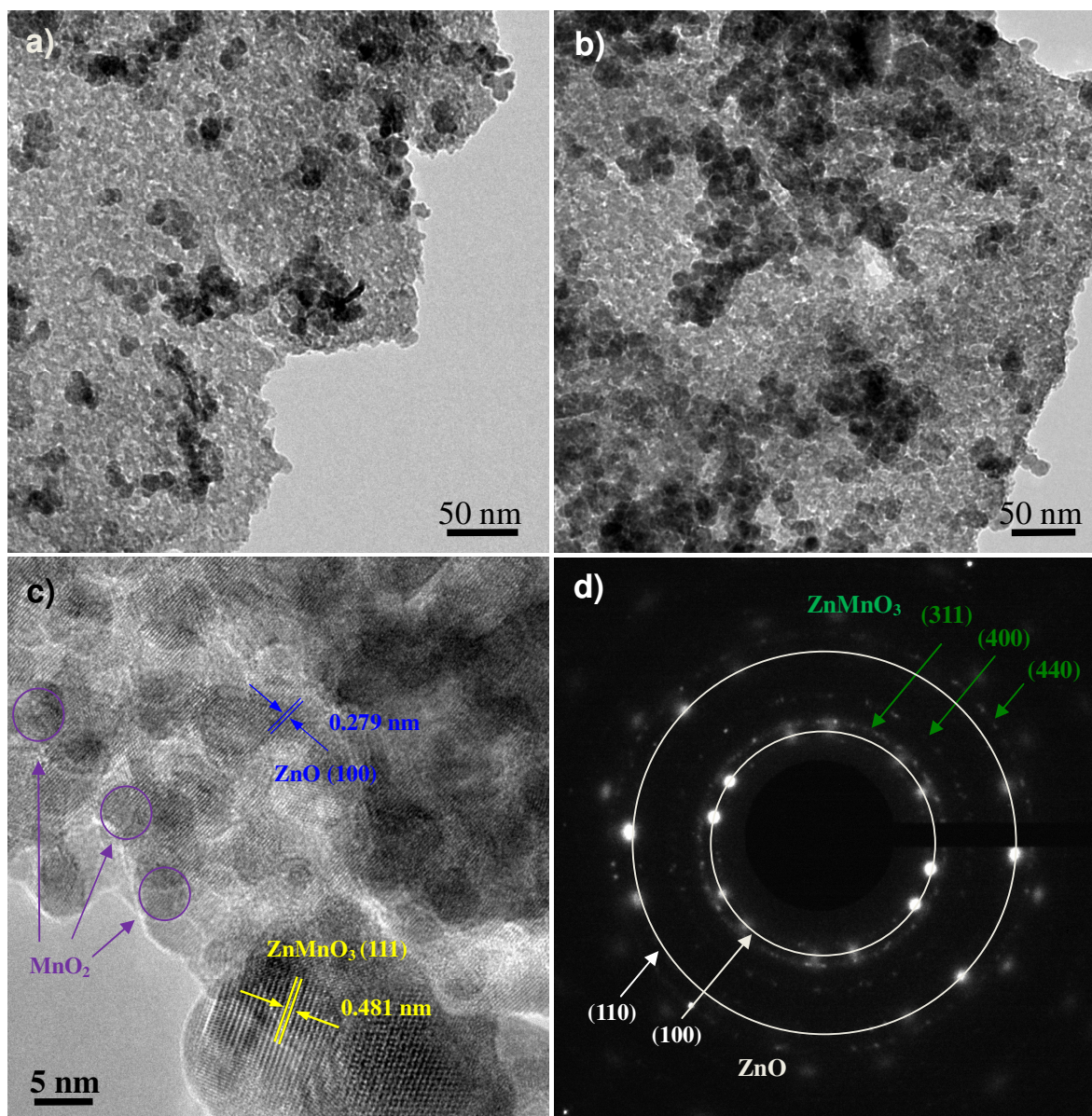


Fig. 3

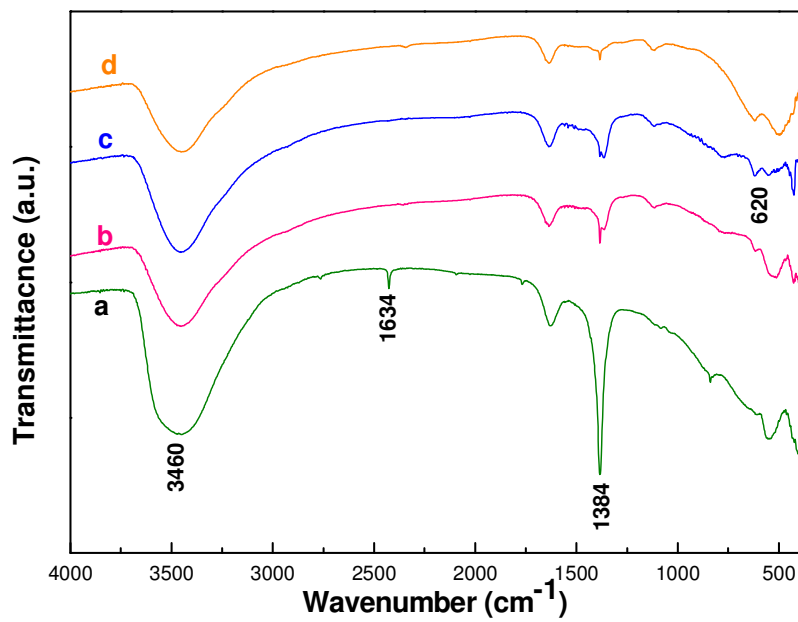


Fig. 4

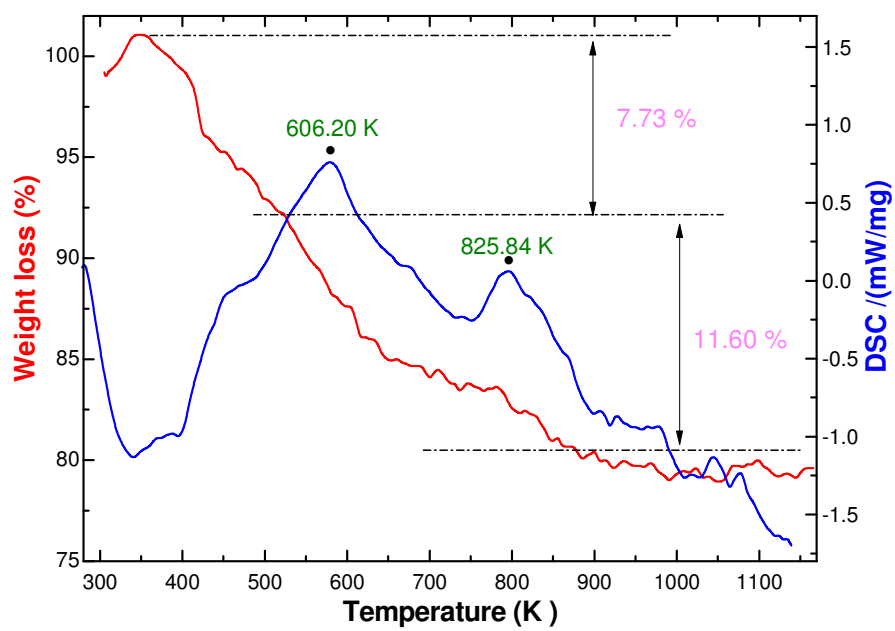


Fig. 5

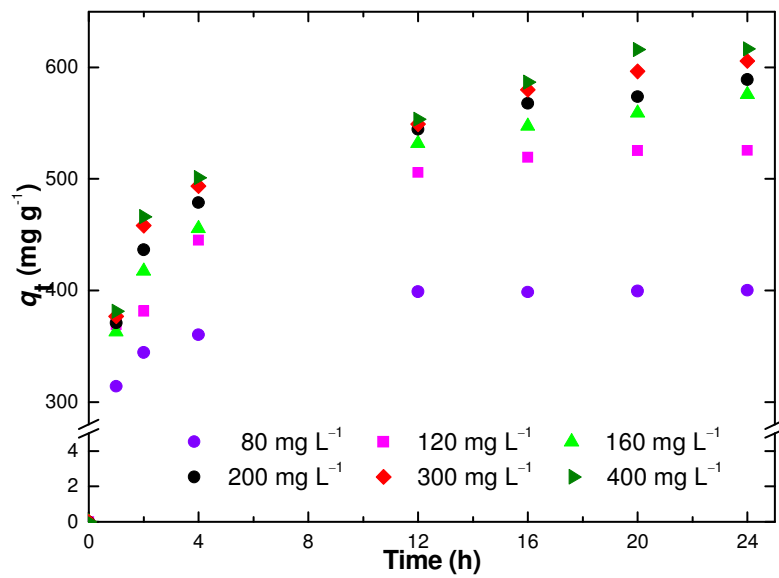


Fig. 6

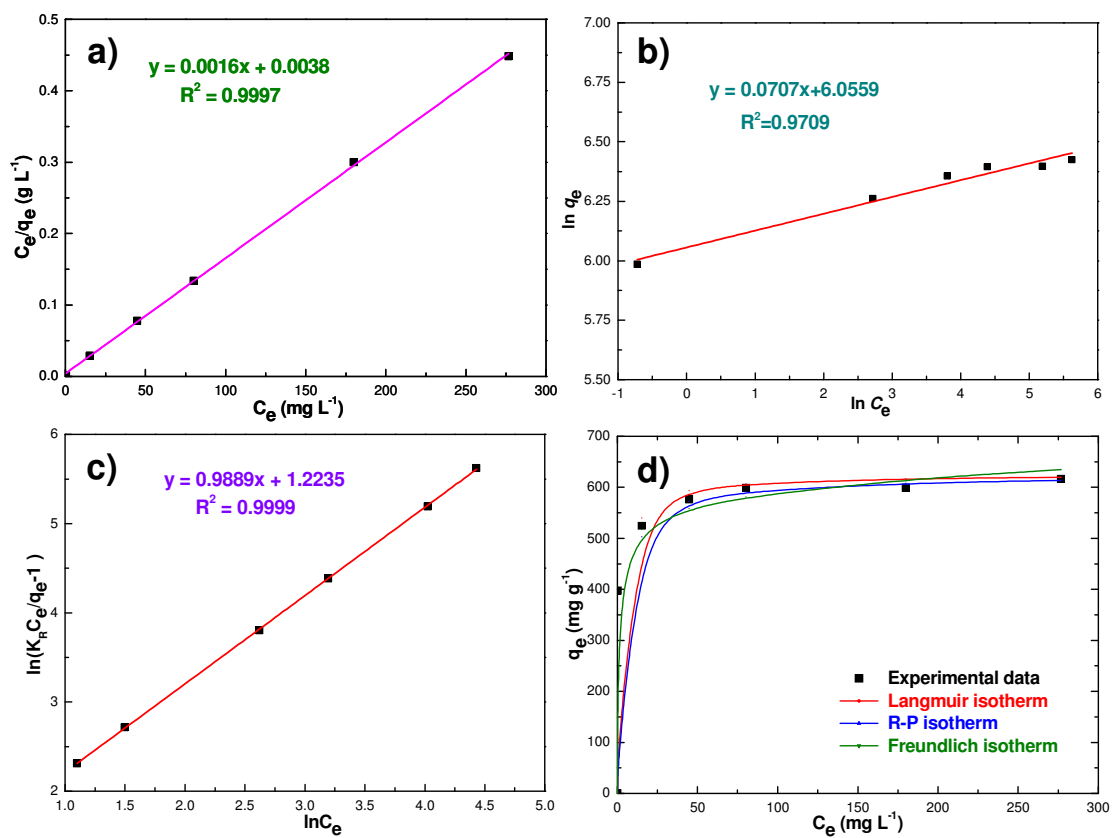


Fig. 7

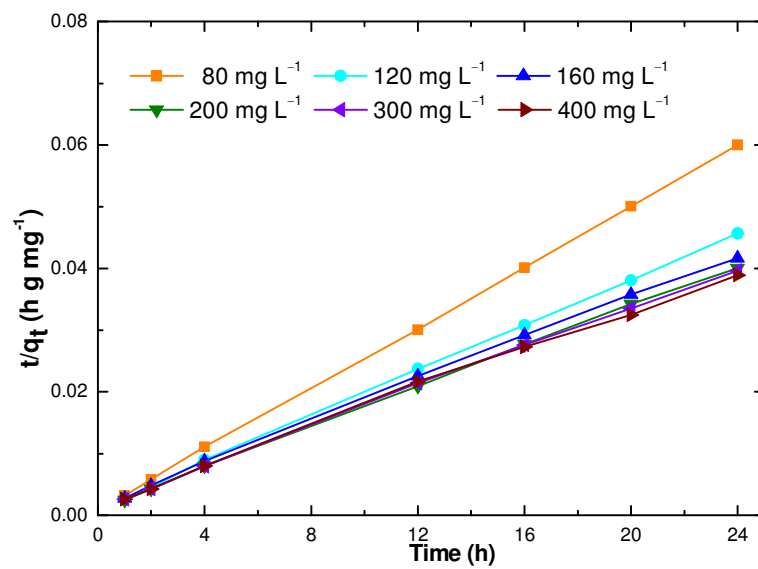
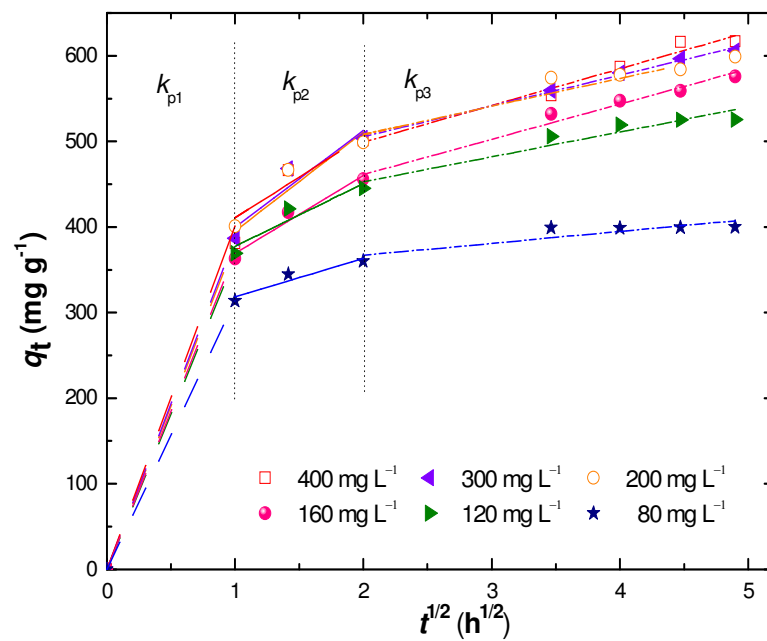


Fig. 8



Manuscript submitted to *Dalton Transactions*.

Fig. 9

